BIS-RS-2017-19

FOSTRAD: An Advanced Open Source Tool for Re-entry Analysis

Alessandro Falchi, Viola Renato, Edmondo Minisci, and Massimiliano Vasile

Aerospace Centre of Excellence (ACE), University of Strathclyde

James Weir Building, 75 Montrose St, Glasgow G1 1XQ. UK

Emails: {alessandro.falchi, viola.renato, edmondo.minisci, massimiliano.vasile}@strath.ac.uk

ABSTRACT

This work responds to the need of modeling the atmospheric re-entry of space debris, satellites, and spacecraft quickly, efficiently and with a reasonable reliability. The Free Open Source Tool for Re-entry of Asteroids and Debris (FOSTRAD) is a simulation suite that allows for the estimation of aerodynamics and aerothermodynamics of an entry object in a continuum or rarefied hypersonic flow by employing the local panel formulation. In this paper, the work done to integrate the tool within a comprehensive framework allowing the simulation of complex geometries using a mesh handler module, a 3DOF trajectory propagator, and a surrogate model generation function, is presented. In addition, a synchronous coupling with a 1D thermal ablation code has been implemented and tested.

The mesh module allows operations such as surface local radius computation, surface facets visibility identification, and objects geometrical evolution due to the burn-up during the re-entry. In the continuum regime, the simplified aerothermodynamics are computed using a local radius formulation, while the tool employs a flat-plate based approach in the free molecular regime. A generalized nose radius-based bridging model has been introduced for the rarefied transitional regime.The tests have demonstrated that applying a local radius formulation along with the radius-based bridging model greatly improves the accuracy of re-entry heat-flux estimations.

The integrated framework has been tested on two different examples of atmospheric re-entries: the ESA Intermediate Experimental Vehicle (IXV) trajectory optimization and the Stardust sample return capsule Thermal Protection System (TPS) burn-up recession; and the coupling between FOSTRAD and the thermal ablation code allowed to study a step-by-step trajectory evolution of Stardust TPS. The obtained results show good agreement with the literature.

KEYWORDS: Atmospheric Reentry; Design for Demise; Survivability; Spacecraft Reentry; Aerodynamic Heating; Ablation; IXV; Stardust SRC.

1. INTRODUCTION

In the latest years the situational awareness on man-made space debris and the application of mitigation guidelines has grown very rapidly. The need of reducing the global space debris population orbiting in the low earth orbit has led to the necessity of developing new satellite design techniques and simulation tools. At the satellite end-of-life, the object orbiting in Low-Earth-Orbit (LEO) usually undergoes an atmospheric re-entry, and the harsh environment (hypersonic velocity and extremely high heating and structural loads) can cause the complete destruction and ablation of the object and its components, making the adoption of a controlled re-entry unnecessary. The Design for Demise is the new design approach aiming at increasing the probability of complete demise during the atmospheric re-entry. The application of design for demise approaches requires methods and tools to reliably quantify the atmospheric re-entry aerodynamics and aerothermodynamic loads. In addition, considering the very high uncertainty involved in the re-entry analyses, it is paramount to quantify also the uncertainty of the investigated parameters and their influence on the demisability of the object.

Aero-thermal re-entry analyses are of utmost importance when design for demise and spacecraft or satellites survivability analyses are pursued. Indeed, in accordance with the NASA-STD-8719.14, every satellite or space structure, whose end-of-life is expect-ably an uncontrolled re-entry, must satisfy the Human Casualty Risk requirements. To assess the re-entry survivability and the related human casualty risk, different software may be used, such as the Debris Assessment Software (DAS) [13] and Object Reentry Survival Analysis Tool (ORSAT)[26] maintained by NASA, or the Spacecraft Atmospheric Reentry and Aerothermal Breakup (SCARAB) [11] currently used by the European Space Agency, or the recently developed Spacecraft Aerothermal Model (SAM)[19].

The latest improvements of the aerodynamic and aerothermodynamic modules within the Free and Open Source Tool for Re-entry of Asteroids and Debris (FOSTRAD)[16] aim at providing the research community a tool to perform quick and reasonably accurate evaluations of different atmospheric re-entry scenarios. With this target in mind, the new updates have been integrated within a holistic framework capable of performing re-entry trajectory propagations, uncertainty quantifications, and atmospheric burn-up of simple- and complex-shaped objects. Since one of the aims is also to use FOSTRAD for the re-entry analysis of space transportation systems, the general framework as been integrated with a module for trajectory optimization, as well.

An object re-entering the atmosphere passes through different flow regimes, each with a decreasing rarefaction degree: Free Molecular Flow (FMF), transitional, slip-flow, and continuum regime. Different high fidelity tools such as DSMC and CFD may be applied in the appropriate regime, even though they can be very computationally expensive. Most low-fidelity tools that model the ablation of re-entering spacecraft are built on the hypersonic local panel inclination method, based on the Modified Newtonian Theory. This approximation provides reasonable aero-thermal results for hemispherical objects, but fails to characterize cubic or sharp-edged objects. In addition, the models are valid only within the continuum regime in a hypersonic/supersonic flow. The low-fidelity models can provide reliable results within the FMF regime by using analytical models, such as the Schaaf and Chambre flat plate model[29]. Characterizing and investigating the transitional and slip flow regime would provide the opportunity to generate more accurate bridging functions[18]. The simplified Newtonian approximation used in the continuum regime, can lead to a misleading heat-flux estimation for flat-surfaced objects (e.g.: flat cylinder, cubes, etc.), with particular reference at the corners proximity. This is due to the fact that when using a constant nose radius, at equal conditions, only the surface inclination influences the heat-flux distribution.

An example is shown in Figure 1, where the experimental data used by Kemp[8] et al have been compared to a test case simulated with FOSTRAD in the continuum regime using a constant nose radius and the very local inclination method proposed by Kemp, Rose, and Detra. Figure 1 shows the relative heat-flux distribution over the normalized surface length. The big discrepancy between the experimental data and the basic simulation approach makes evident that the constant radius formulation completely fails to identify the local increase of the heat-flux at the rounded corner. In fact, the flow is mostly subsonic at the stagnation point, whereas when the considered point moves closer to the object's edge the flow accelerates due to the expansion that takes place at the corners. The complex phenomena taking place at the sharp-edged corners cause the local similarity assumption, on which the simplified theories are based, to fail. Some examples representative of the phenomena for cylinders and cubes simulated via CFD have been reported in [2].

In the last years, different solutions, or mitigation strategies, for increasing the accuracy of the local panel inclination methods have been proposed. Merrifield[19] applied an experimental-based approximation for flat-ended cylinder developed by Klett[10]. A viable but computationally expensive solution valid in the slip-regime has been proposed in [5], consisting in the generation of a Direct Simulation Monte Carlo (DSMC)-based model for estimating the surface heat-flux distribution at different attitudes. Even though, the use of DSMC methods in the slip-regime could be very computationally expensive, and unfeasible without the use of a high-performance computer, the approach has been taken under consideration. In fact, as it is reported in [6], the use of low-fidelity DSMC simulation can lead to predictable errors and reasonable surface heat transfer estimations with a decreased computational cost. Another approach to the problem is the one preliminary proposed in the PAMPERO tool, developed by the CNES[1], using a local radius formulation.

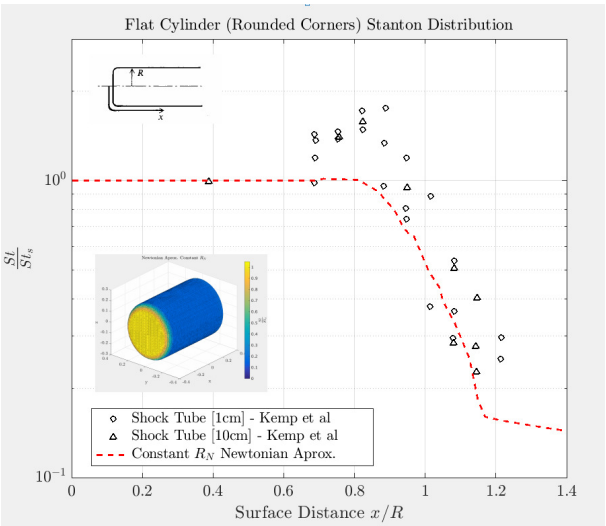

Figure 1: Constant nose radius problem: Heat-transfer distribution on a flat-nosed body with rounded corners.

In the present study, the latter approach has been considered and a dedicated surface local radius algorithm with the aim of further increasing the accuracy of this method has been developed. In the second section, the overview of FOSTRAD is presented, describing the latest updates, where particular attention is given to the local radius computation algorithm, which has been created in order to be flexible and computationally efficient. In the third section, the 1-D thermal ablation code, which has been coupled to FOSTRAD, is briefly described. The following two sections focus on the application of the framework to study the Experimental Intermediate Vehicle (IXV) re-entry trajectory optimization, and the Stardust sample return capsule (SRC) thermal protection system ablation prediction. In addition, the new integration of the surrogate modeling, uncertainty quantification, and trajectory propagator tools is briefly described within the study cases. A section with conclusions and ideas for future works ends the paper.

2. FOSTRAD: LATEST DEVELOPMENTS

The Free Open Source Tool for Re-entry of Asteroids and Debris[16] was initially implemented for the fast characterization of the aerodynamics and aero-thermodynamics performance of simple shaped objects, which could preliminarily represent space debris or meteoroids. With the recent improvements on the aerodynamic module, the software can simulate complex geometries with a very good accuracy[7]. Given the computational efficiency of the tool, FOSTRAD had been coupled with uncertainty quantification tools, allowing the software to take into account aleatoric and epistemic uncertainties of (re-)entry scenarios[18].

The tool has proven its suitability also for studying space debris re-entry ground footprint estimation[17]. FOSTRAD requires inputs such as the object geometrical model, orbital altitude, attitude, and gas-surface interaction parameters such as the molecular diffusive accommodation coefficient. Then, by using a reference atmospheric database, it computes all the flows properties required for running the simulation, such as density, viscosity, mean free path, temperature. After the initialization, the tool identifies the visible facets, which are then used to run the local panel analyses. The visibility facet detection algorithm employs a fast and advanced attitude depended method, based on two different techniques: the occlusion culling and back-face culling[7]. This approach gives the capability to detect the mutual shadowing of single-body and multi-bodies assemblies. Which is going to be employed for future debris re-entry assessments.

FOSTRAD performs the aerodynamic analyses depending on the flow regime, identified by the Knudsen number (Kn). In the continuum regime (i.e.: $Kn <= 10^{-3}$) the Modified Newtonian Theory is used, as proposed by Lees[12]. In the rarefied regime ($Kn >= 100$), the Schaaf and Chambre inclined flat-plate model[29] is employed. In the transitional regime, FOSTRAD uses a set of generalized and object-specific aerodynamic bridging functions. The aerothermodynamic analyses may be performed choosing among different heat transfer formulations: Lees's[12], KRD [9], Van Driest[32] and the equivalent KRD formulation as implemented in SCARAB[11].

This work focuses on the improvements of FOSTRAD's aerothermodynamics module, which has been updated with a local nose radius formulation that is computed with a dedicated algorithm. This approach, only apparently a minor and trivial change, is in fact a big step forward, requiring the use of a complex mesh-handler and bridging model which takes into account the radius assigned to each facet. At the same time, the use of a local formulation requires the introduction of a local temperature distribution, which is also employed by the coupled thermal ablation code.

2.1. Local Radius Computation Algorithm

The algorithm has been specifically studied for the integration in FOSTRAD. Indeed, the curvature computation is performed on a stereolithography (STL) model, which can be a simplified triangulated surface of the satellite or space object to be simulated. The STL file contains all the information to build an unstructured triangular mesh: points coordinates, points connections for each facet, and also the normals of each facet. FOSTRAD's mesh module is able to handle also general polygonal models, which are then processed as triangulated STL files. The local radius computation module is based on the curvature estimation algorithm proposed in [28]. The curvature algorithm computes the estimated principal Gaussian curvatures for each vertex of the STL mesh. The curvatures are estimated locally on each different facet. The computation is based on the change of the normals from a face to their neighbors. The triangulated mesh allows the computation of the facet normals, from these, it is possible to average neighbors facets normals and obtain the per-vertex normals. The normals averaging is performed according to the methodology proposed in [15]. The local curvature radius at each vertex is then defined by the general Gaussian principal curvatures relation:

$$R_i = \frac{1}{\sqrt{\kappa_{1,i}\kappa_{2,i}}} \tag{1}$$

where R_i is the i-th vertex average local radius, κ_1 and κ_2 are the principal Gaussian curvatures. In its form, the algorithm allows for the computation of the curvature just by taking a ring of neighbors around each vertex, for complex objects, leading to local vertex or face radii that will present very steep variations. In addition, the radius for a flat surface is obviously infinite, therefore, a fixed reference local radius is applied on the "flat" vertexes or facets. As reported by Klett[10] in his the experimental findings, the flat-ended cylinder had a stagnation heat-flux which was half of the equivalent sphere-radius stagnation heat-flux. Therefore, the reference flat-surface radius, was set to be equal to the reference length of the object. E.g.: for a flat-ended cylinder in a head-on flow it would be the diameter, which would lead a stagnation point heat-flux half of the equivalent hemispherical-ended cylinder or sphere in equal conditions.

For the actual implementation of the algorithm, a mesh preprocessing phase is required, because the mesh must be manifolded (i.e.: each edge is part of two facets), with unique vertexes coordinates, and completely connected.

The local radius estimation algorithm includes different setup parameters in order to be flexible and allow the user to calibrate the local radius distribution on the expected continuum heat-flux distribution for complex objects. Indeed, computing the radius-on-vertex using just 3 normals, may cause the following problems:

1. Sharp edges and corners identified with a very low local radius $R_i \longrightarrow 0$
2. Flat facets defined by $R_i \longrightarrow \infty$
3. Non-flat facets recognized as flat (for meshes with a high resolution)
4. Radius distribution highly dependent on the mesh
5. Local discontinuities on the edges (due to the use of the mean Gaussian curvature)

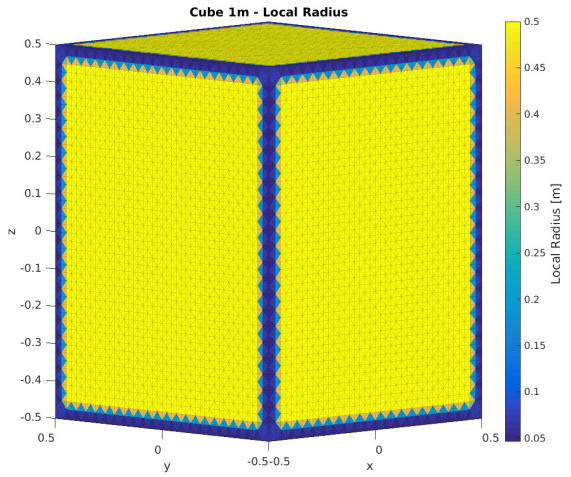

Figure 2: Non-smoothed local radius distribution for a cube.

An example of how a non-smoothed local radius distribution would look like is shown in fig. 2. Where a 1m cube object has been used as initial test, and the flat-faces had been assigned with a $R_i = 0.5$. The local curvature on the edge is automatically conditioned by the algorithm, as normally, on the edges (and not on the corners) only one facet every two consecutive would have a finite mean Gaussian curvature. As the reader can easily observe, this distribution is very far from being a realistic representation of a continuum heat-flux distribution[2].

In order to provide a better and consistent heat-flux representation, a local property smoothing function has been integrated within the radius distribution algorithm. The local smoothing function structure is represented in Figure 3. The smoothing algorithm has been implemented with a modular structure, therefore, it can be used also for smoothing different surface properties (not only the radius). Among the inputs there is the mesh triangulation, the reference minimum and maximum radius, and a set of smoothing parameters which will be just briefly described, as their complete explanation would go out of the scope of this work. The most important parameters are the following:

- N_{smooth}: number of closest points to be smoothed
- averaging type: simple or exponential moving average (weighted or not)
- *Flat Edge*: edge value on the ratio between flat-facets and N_{smooth}
- Flat faces weighting method: linear or sigmoid

The main surface smoothing parameter is the number of closest vertexes (or facets) properties to be averaged (N_{smooth}). The algorithm recursively detects the N_{smooth} closest points around each *i-th* vertex, and computes their average according to different averaging strategies, such as a simple or exponential moving average based on the sorted distances from the *i-th* element.

The Flat Edge parameter is the limit value that is used to determine whether a facet (or a vertex) radius should

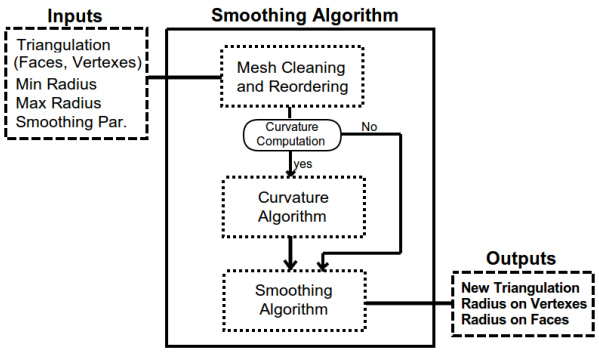

Figure 3: Smoothing algorithm block diagram.

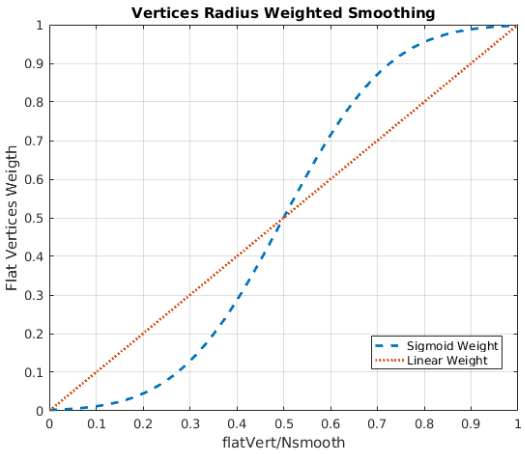

Figure 4: Linear and sigmoid flat-face reference value weighting function.

be considered as "flat" or not. Precisely, for each mesh facet the algorithm identifies, among the closest N_{smooth} facets, the number of facets having a "flat reference value" and computes "flat-facets-ratio" as the ratio between the number of flat facets and the total number of smoothing points:

$$F_{R,i} = \frac{N_{flat,i}}{N_{smooth}} \tag{2}$$

where $F_{R,i}$ is the "flat-facets-ratio" of the considered i-th facet, and N_{flat} is the number of the flat facets identified among the closest N_{smooth} facets. Afterwards, if the $F_{R,i}$ is higher than the Flat Edge input, the facet is considered as flat and it is assigned the flat radius reference value. Otherwise, the radius averaging among the closest N_{smooth} points is computed. The averaging process can either be weighted or not weighted; in this specific case the weighted average is not intended as a classical weighting process. In this context, the the "weight" is assigned only to the $N_{flat,i}$ facets; while an unitary weight is assigned to the non-flat facets.

The previous definition of weighting implies that only the flat facets are weighted (in a scale from 0 to 1), directly depending on the $F_{R,i}$, and as already stated, the closest flat-edged facets are weighted only if the $F_{R,i}$ is above the Flat Edge input parameter, otherwise they are assigned with a reference flat-radius value. This weighting

process has been proven to be the most appropriate for representing a hypersonic heat-flux distribution on flat-surfaced objects. The weighting function can either be linear, or sigmoid-shaped (Figure 4, the reader can observe that the x-axis is displayed as the number of flat vertexes to the total number of averaging points, which is exactly the $F_{R,i}$. The sigmoid weighting function has been defined in order to obtain an better radius distribution at the sharp corners, and a smoother transition to a flat surface. When compared to the linear bridging function, the sigmoid provides a lower radius at the corners and a higher radius as the point moves away from an edge or a corner. An example of the different surface smoothing weighting methods is shown in Figure 5.

The algorithm has been tested on many different complex shapes and the radius distribution has been validated on simple geometries (i.e.: ellipsoids, spheres, etc.), and the results have been proven to be reliable, consistent and efficient. Moreover, to allow for a better flexibility, the code had been improved with a concave-convex edge filter. The entire process (curvature computation and smoothing process) generally requires around 3s every 10 000 facets running on a common contemporary workstation, making it suitable for the integration within FOSTRAD. If a mesh with a high number of facets (e.g., 50 000) is detected, in order to keep the computational time short, the tool automatically switches to a parallel computation. In order to give a better accuracy, the algorithm allows the user a certain flexibility on the initial smoothing parameters initialization; in this way, if the user has the access to high-fidelity tools or experimental data, he/she would be able to perform an ad-hoc calibration. Otherwise, as it has been drawn as conclusion of this work and is hereby discussed, the user can use the recommended setup for different classes of identified geometries:

- Hemispherical shapes: low $N_{smooth} \approx 3/1000$,
- Objects with flat faces and rounded corners: medium $N_{smooth} \approx 10/1000$,
- Complex objects with sharp edges and flat faces: low $N_{smooth} \approx 25/1000$,
- For all geometries, the "Flat Edge" parameter should be above 0.70 in order to prevent steep variation from flat regions to non-flat regions (e.g.: rounded corners)

Where N_{smooth} is expressed as number of smoothing points per 1000 facets. In this specific work, the smoothing algorithm parameters have been preliminarily calibrated on the flat-ended cylinder and the IXV geometry. All the analyses in this work have been performed using the exponential moving average and the sigmoid weighting function smoothing and the surface inclination distribution have been computed using Kemp, Rose, and Detra model.

In Figure 6, the comparison between the experimental data used by Kemp[8] et al and the analysis performed with FOSTRAD employing the smoothed-local-radius formulation is shown. The comparison between Figure 1 and Figure 6 makes evident that the local radius formulation provides an accuracy far better than the constant nose radius approach, especially at the rounded corner. In Figure 6, it is also reported the influence of the various setup parameters, i.e.: N_{smooth}, and the Flat Edge (identified as FF). The result shows that, for a geometry without sharp edges, a possible setup configuration would be using $N_{smooth} = 10/1000$ and a Flat Edge = 0.8.

In Figures 7 and 8, a preliminary calibration of FOSTRAD local radius formulation setup on the IXV geometry is reported. The relative heat-flux distribution of CFD data provided by Roncioni[27] et al. is compared to different N_{smooth} values. It is shown that for a complex geometry with sharp corners, a higher number of smoothing point should be used (the best fit is shown using 30 smoothing points per 1000 facets), the analysis has shown that the optimal flat-edge was between 0.75 and 0.9. The comparison shows also the underestimation of the relative heat-flux on the flaps. This could be due to very high heat-flux on the flaps due to the shock impingement and a different flap inclination angle. Additionally, in the quest of finding alternative methods for calibrating the local radius smoothing algorithm, a very low-fidelity DSMC simulation was run at the same CFD conditions simulated by Roncioni, using a mesh with the same number of cells (i.e.: 2 millions cells). Surprisingly, even though the absolute heat-flux values are completely different, the relative heat-flux distribution computed by the dsmcFoam code is very close to the CFD one, except for the flaps region, as the DSMC could not be able to properly resolve the shocks impingement and interactions. The advantage of using a low-fidelity DSMC simulation to calibrate the smoothing algorithm would be that a DSMC simulation requires a systematic setup, and additionally, FOSTRAD had already been coupled with the dsmcFoam code via an automated simulation interface[6], which could lead to an automated calibration process for any geometry. Even though the DSMC simulation would be low-fidelity, that would still require the use of a High Performance Computer.

More DSMC simulations were performed on the flat-ended cylinder; another example has been shown in Figure 9, where a simple sensitivity analyses had been performed on the Mean Free Path to cell size ratio (MFP/C_x). This ratio, as a good practice, should fall between 2 and 3[30], whereas in this work a MFP/C_x between 0.05 and 0.15 has been used, therefore the simulations are considered as "low-fidelity". It is possible to observe a good agreement between the experimental data and the DSMC relative heat-flux distribution. Moreover, as it would have been expected, increasing the MFP to cell size ratio increases the accuracy of the DSMC relative heat-flux distribution. These simulations were performed in a slip flow regime ($Kn = 2.5{\cdot}10^{-3}$). These results suggest that even though a low-fidelity DSMC simulation cannot provide any accurate estimation of the absolute heat-flux in the continuum regime, it could be used to evaluate a reasonable relative heat-flux distribution.

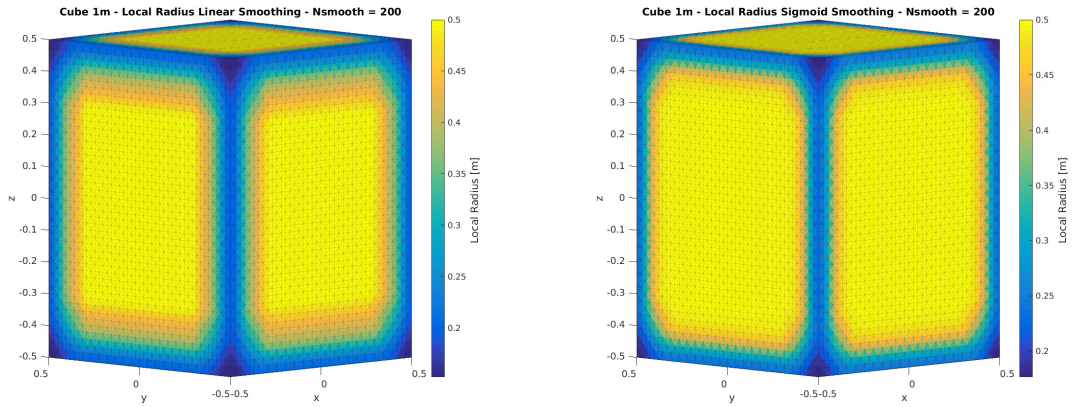

Figure 5: Local radius distribution, exponential smoothing linear-weighted (on the left) and sigmoid-weighted (on the right)

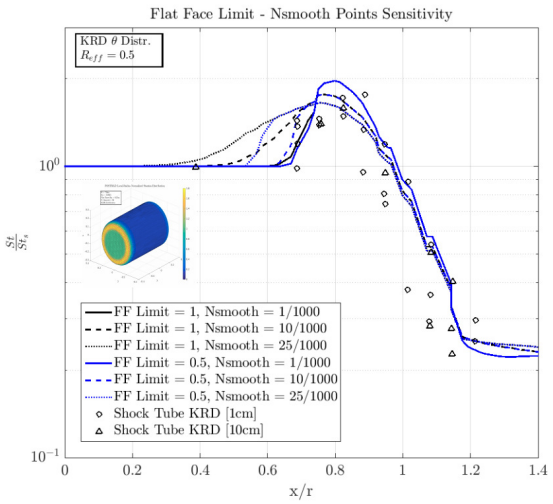

Figure 6: FOSTRAD relative heat-flux distribution computed with the smoothed-local radius formulation, compared to the experimental data reported in [8].

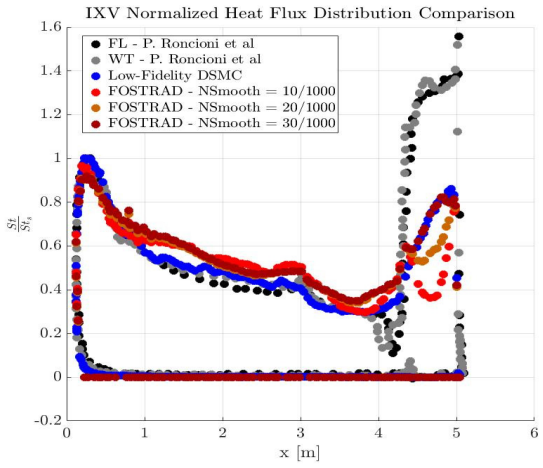

Figure 8: Relative heat transfer coefficient distribution comparison of CFD, DSMC and FOSTRAD data on the IXV model. Sensitivity analysis on the number of local radius smoothing points.

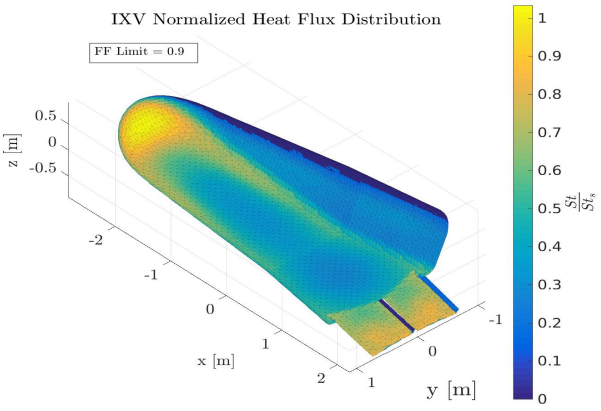

Figure 7: FOSTRAD relative heat-flux distribution: hypersonic continuum regime with local radius formulation.

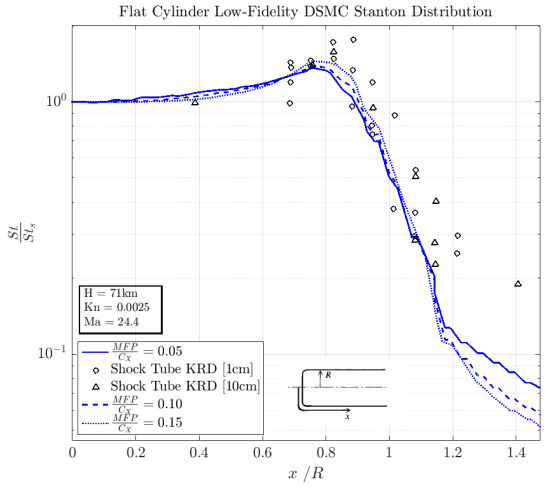

Figure 9: Relative heat transfer coefficient distribution comparison of experimental data[8] and a sensitivity analyses performed on different low-fidelity levels DSMC simulations.

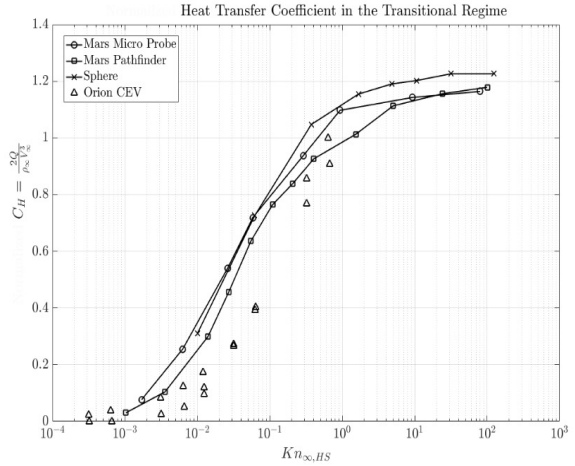

Figure 10: Heat transfer coefficients for different re-entry scenarios and objects characterized by a different nose radius

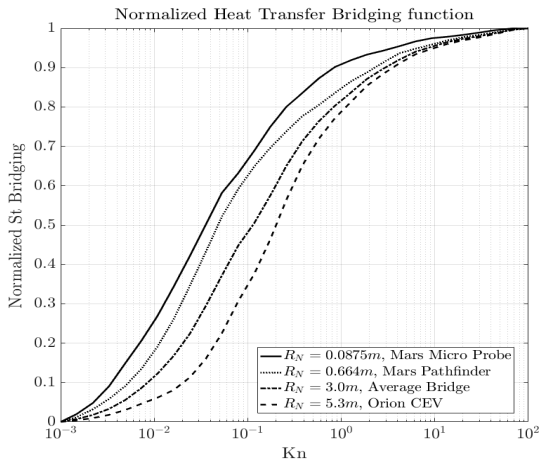

Figure 11: Normalized bridging functions for different space objects and scenarios, characterizing the geometries with different nose radius.

2.2. Local Radius-Based Bridging Model

The introduction of the local radius formulation for the aerothermodynamics module leads to the need to change the rarefied transitional regime heat-flux computation. Indeed, the local radius formulation implies that in the continuum regime, beside the atmospheric properties, the heat-flux is going to be computed as a function of the *i-th* facet radius and inclination. In the free molecular regime the heat-flux is radius-independent, implying that the transitional bridging model had to shift from a radius/inclination-based model in the near-continuum regime to a inclination-based model in the near-free-molecular regime.

By comparing the data of different re-entry heating analyses for geometries with a different effective nose radius, it is evident that using the same bridging function for different nose radius would not bring to accurate results, as it is highlighted for the Mars Pathfinder[20], Mars Microprobe[21], a 1.6m diameter sphere simulated by Dogra[4] (which were extended with a set of in-house performed DSMC analyses), and the Orion Crew Exploration Vehicle[16] shown in fig. 10. In addition, considering the continuum and free molecular transitional regime boundaries to be respectively $\mathrm{Kn_c}$ = 0.001 and $\mathrm{Kn_{fm}}$ = 100, the heat transfer coefficient derivative over Kn is different for different effective nose radii; therefore, using an averaged bridging function would cause discontinuities at the two transitional regimes boundaries. Considering only the reference data falling within the transitional regime, and creating the bridging models the differences are more evident (fig. 11).

Due to the previous consideration, a more accurate bridging model as a function of Kn and the effective nose radius has been proposed. The model has been created using a recursive 1-D Piecewise Cubic Hermite Interpolation on referenced data, and it is shown in Fig 12. The bridging model is applied as it follows:

$$St_{i,t} = St_{i,c} + \mathbb{B}(R_{N,i}, Kn) \cdot (St_{i,fm} - St_{i,c}) \qquad (3)$$

Where *St* is the Stanton number, *i* refers to the *i-th* considered facet, the subscripts *c*, *t*, *fm* refer to the continuum, transitional, and free molecular regime respectively, $\mathbb{B}$ is the developed bridging model, and R_N is the local nose radius.

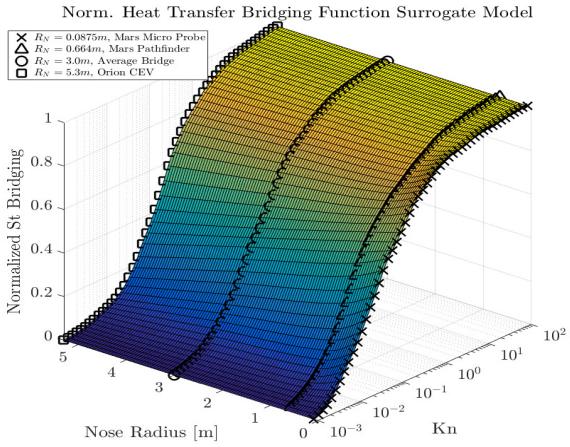

Figure 12: Transitional regime normalized bridging model as a function of the local radius and Knudsen number.

The newly introduced bridging model formulation, allows FOSTRAD to operate using the multi-threaded computation on all the facets and given trajectory parameters. Once the mesh has been initialized (depending on the required resolution the initialization usually requires from 2 and 10 seconds), and for a constant space object attitude, it usually takes less than 1 second to compute the the aerodynamics and aerothermodynamics, including the heat-flux surface distribution for each and every trajectory point given as input, on a machine operating with an Intel® Core™ i7-4790 CPU 3.60GHz x8.

3. THERMAL ABLATION CODE

The code used to produce the ablation simulation is a one dimensional code based on the implicit finite differ-

ence method. This code has the capability to estimate the pyrolysis phenomenon progression and the consequent changes of density and temperature in the thermal protection material. The program governing equations are briefly illustrated in the following section. The capability of the code to produce reliable re-entry results has been proven for both Earth re-entry [25] and Martian entry [24].

The program is based on three main equations. The first one is the Arrhenius equation which describes the ablator degradation rate and calculates its density and change of state at every time step. The second equation is the in-depth energy equation, which represents the different energy rates existing inside the ablative material, e.g.: the storage of sensible energy, the thermal conduction and the pyrolysis energy consumption. The last main equation is the energy balance at the external surface which calculates how much of the heat flux estimated by the aerodynamic model reaches the material external surfaces and influences the ablative process [22]. A precise material model containing the thermochemical properties of the material, e.g.: the specific heat flux, the thermal conductivity, the density and the pyrolysis characteristics, is essential to produce accurate simulations of the thermal protection system behaviour. These properties are empirically estimated during extensive and expensive characterization campaigns by the material producer; that is the reason why it is not always possible to find exaustive data in literature.

In the case of the IXV simulation a non ablative material has been selected to better represent the real thermal protection system materials used in this vehicle. Unfortunately, to the authors' knowledge, the thermochemical characteristics of the real materials used are not available in literature; therefore an approximated material model has been generated to produce the IXV re-entry. Stardust fore-body was made of an ablative material called PICA, Phenolic-Impregnated Carbon Ablator. A number of adequate thermochemical models are present in literature for this specific material, the most complete of those was selected for the Stardust re-entry analysis. In both test cases a singular material was utilized to characterize the entire geometry of the spacecraft; it was decided to do so for simplicity of the model and lack of information regarding the real materials properties. In reality both spacecraft used different materials in different part of the geometry; in case the full set of data for the materials becomes available the code is already capable to simulate a multi-material geometry.

4. IXV RE-ENTRY TRAJECTORY OPTIMIZATION

In this section, the application of FOSTRAD to study the re-entry phase of the Intermediate Experimental Vehicle (IXV) is described. The IXV project was intended to be a re-entry technology demonstrator with a particular focus on aerothermodynamics and thermal protection systems (during the re-entry, IXV was expected to reach wall temperature up to 1700^oC). The purpose of this study

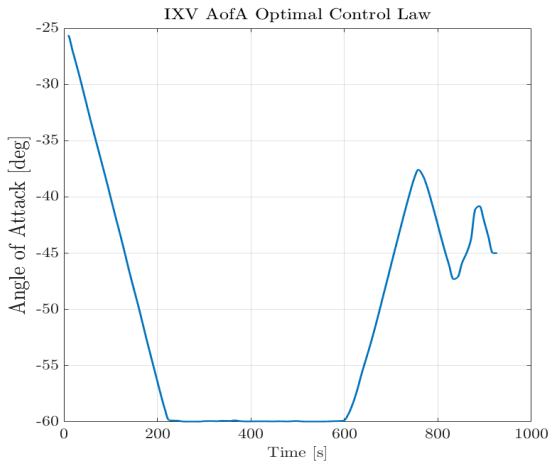

Figure 13: IXV Trajectory optimization: angle of attack optimal control law.

case was to highlight both FOSTRAD aerodynamic and aerothermodynamic accuracy, while testing also its computational efficiency and the overall software stability.

The problem was defined as the optimal control problem for the angle of attack of IXV re-entry trajectory, with a single objective function which was defined as the total surface heat-flux integral over the trajectory. The heat-flux was computed using the newly implemented local radius formulation and the KRD supercatalytic wall formulation, with the smoothing calibration parameters identified in the previous section (i.e.: $N_{smooth} = 30$, and Flat Edge = 0.8). The nominal trajectory parameters[27]: initial entry altitude was 120km, flight path angle of -1.6deg, and an initial velocity of 7400m/s. The target trajectory parameters were set to a velocity of ≈450m/s (equivalent to a Mach ≈1.5), an altitude of 25km, and an angle of attack of 45deg, which was a boundary condition required for allowing the deployment of parachutes. The optimization was performed using a Multiple Shooting method[14]. Constraints were imposed on the acceleration (axial an vertical equal to 3g and 1.5g respectively) and the angular velocity on the angle of attack of 10deg/s. An additional constraint was set on the maximum stagnation heat-flux, equal to 100W/cm^2.

In order to make the optimization computationally efficient, the coupling between FOSTRAD and the optimization tool is performed through a surrogate model of the total heat-flux absorbed by the spacecraft per unit time. FOSTRAD is first used to create the surrogate model of the total absorbed heat-flux as a function of altitude, attitude, and velocity. The same surrogate model function used in this step, may be used for performing uncertainty quantification analyses[7]. After the optimization is completed and the optimal control law is obtained, FOSTRAD is directly used to perform the entire trajectory propagation, creating a dataset to be analyzed. During the last trajectory propagation, FOSTRAD is coupled with the thermal code, which computes the temperature propagation within IXV thermal protection system layers.

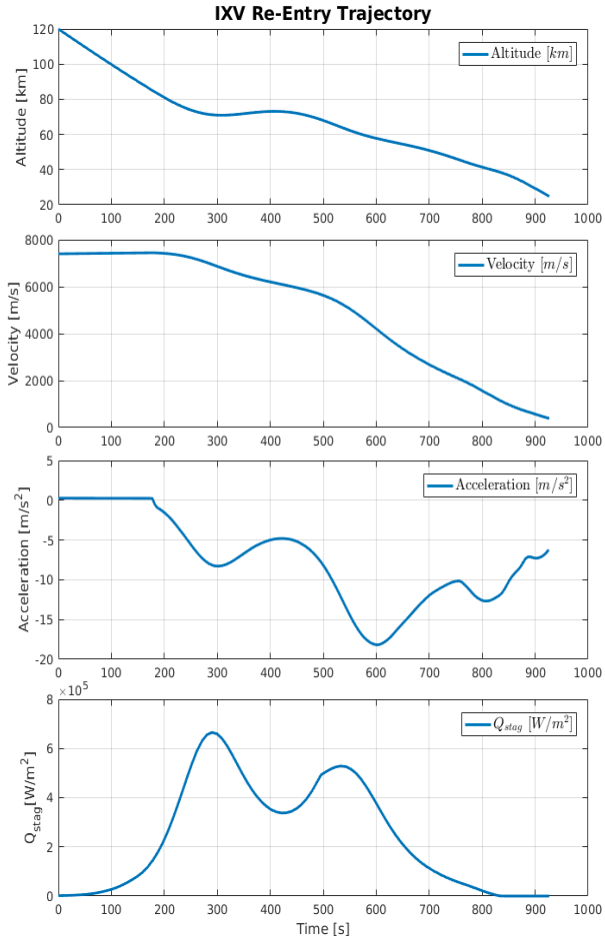

Figure 14: IXV atmospheric re-entry: heat-flux optimized trajectory.

Several optimization trials have been run with different first guesses, and a convergence was found with the optimal control law shown in fig. 13. The trajectory overview is illustrated in fig. 14 (only the vectorial acceleration and not its components have been shown). An example of the maximum temperature reached during the trajectory is shown in fig. 15, which is slightly lower ($\approx$6%) than the nominal temperature peak of 1700^oC.

5. STARDUST TPS AEROTHERMAL ABLATION

The newly updated FOSTRAD aerothermal module and the coupling with the thermal ablation module allows the study of ablative (or non-ablative) thermal protection systems. The Stardust sample return capsule (SRC) was identified as a suitable test case for the coupling, due to the extensive dataset available. Stardust is a small robotic probe (weighting just 46kg) that was designed for a flyby to the comet Wild 2 in order to collect dust samples and return them on the earth. The capsule was expected to re-enter the atmosphere with a very high velocity 12.8km/s, a flight path angle of -8.2deg[3], the entry interface was assumed at 125km, and the attitude was fixed at 0deg. The trajectory was stopped around the expected hypersonic drogue opening altitude and speed, which were 32km and Mach 1.37 respectively.

Initially, the re-entry trajectory analyses were performed using the previously integrated 3DOF tool and FOSTRAD. Since the thermal analyses performed with the thermal ablation code are computationally expensive, and no major alterations of the aerodynamic properties were expected due to the ablation, the trajectory was obtained with the ablation code switched-off. The trajectory results are shown in fig. 16. The results show a very good agreement with the analyses reported by Desai[3] et al. Different parameters for the Stardust trajectory had been considered by Olynick[23] et al, even though they still compare well with FOSTRAD results. The acceleration curve reported in fig 16 is in agreement with the maximum acceleration peak of 38.1g reported by Willcockson[34].

A more detailed comparison on the aerothermal data reported by Olynic[23] and Trumble[31] was performed: the different aerothermal models that had been integrated in FOSTRAD have been tested at the same condition as the ones reported by the two authors, and the results are shown in Figure 17. The comparison highlights what follows (note that some of the comments can be seen as confirmation of what already is known):

- Van Driest model can be conservatively used for design for demise re-entry analyses as it represents the lower heat-flux boundary
- SCARAB model shows the highest heat-flux estimation, representative of a supercatalytic wall condition. It can be conservatively used for TPS burn-up estimation
- Kemp Rose Detra and Fay Riddel models fall between the highest and lowest boundaries, and in

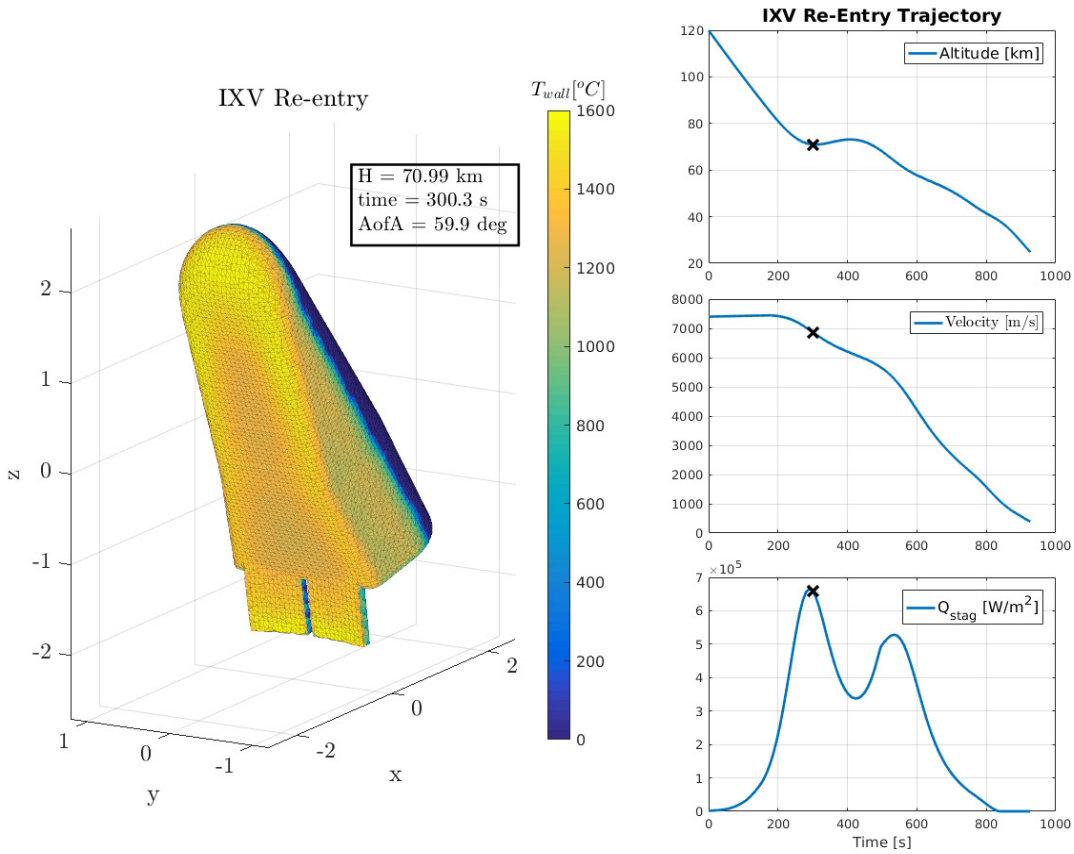

Figure 15: IXV atmospheric re-entry: surface temperature distribution computed by FOSTRAD and the coupled thermal code.

FOSTRAD they are implemented with a fully catalytic wall condition.

- Kemp Rose Detra and Fay Riddel models fall between the highest and lowest boundaries, and in FOSTRAD they are implemented with a fully catalytic wall condition.

The analyses shown in Figure 17, do not include the radiative thermal heat-flux, which is computed by the thermal ablation code.

Another interesting result is the comparison between the heat-flux distribution computed with FOSTRAD and by Trumble[31]. The results highlight that FOSTRAD compares well on the fore-body, even though it shows a significant heat-flux overestimation on the shoulder radius. In addition, the picture shows an x-axis off-set between the two shoulder heating peaks, this is due to a slightly different geometry (Figure 19). The offset of the geometric position of the shoulder is roughly the same as the one shown by the peak heat-flux. Therefore, it can be concluded that with the same geometry the heating peaks would have been computed at roughly the same x-axis length.

To simulate the actual burn-up, FOSTRAD has been run with SCARAB aero-thermal model[11], using the trajectory parameters (i.e.: altitude, velocity) previously computed, and a constant angle of attack of 0deg. The real-time coupling between FOSTRAD and the thermal ablation code granted that every geometrical feature change was correctly captured (i.e.: surface inclination and local-radius variation). Indeed only a step-by-step geometrical evolution is able to expose new facets to the flow, e.g.: as the rounded corners tend to recede, they leave new facets exposed to the aerothermal flux. In Figures 20 and 21 are shown two different time steps of the actual atmospheric re-entry simulation, the heating peak and the final time step respectively.

It is interesting to observe how the recession progressively exposes facets that were shadowed by the corner, and the code is able to accurately adapt the mesh evolution. By analyzing the actual stagnation point heating, it is possible to observe some small fluctuations at the peak. This is most likely due to the input data used for the simulations, which showed small fluctuations on the velocity, then amplified on the heat-flux. The final geometrical shape is representative of the actual model that was tested for the aerodynamic stability during the pre-drogue triggering phase by Willcockson[34] et al.

The analyses on the Stardust re-entry maximum and average wall temperature shows a good agreement with the telescope observation reported by Winter[35] et al (Figure 22). FOSTRAD averaged temperature have been computed on the fore-body only. Although, it is possible to observe an off-set on the altitudes at which the maximum temperature occurs. This may be caused by trajectory parameters used for simulating the re-entry; an example

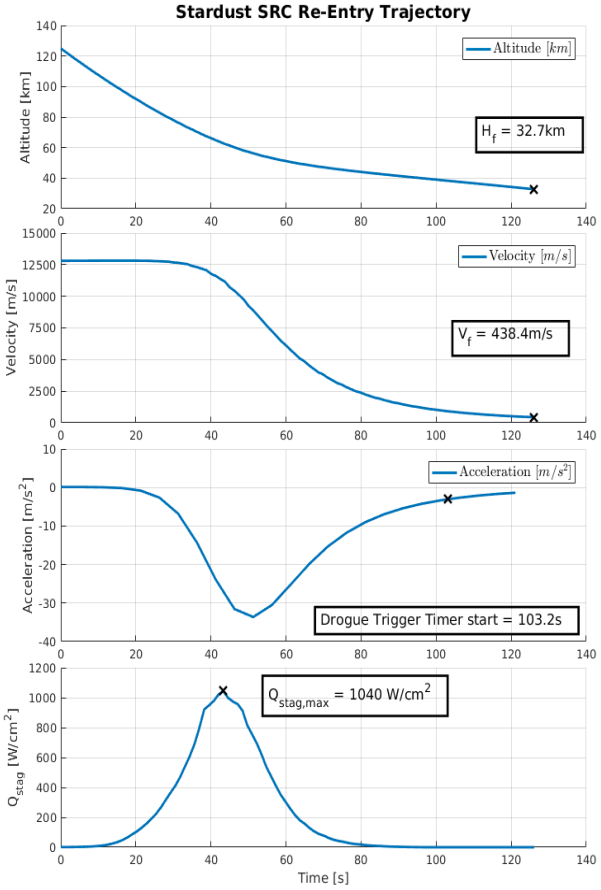

Figure 16: Stardust atmospheric re-entry simulated with FOSTRAD using 3DOF, highlighting different representative points: final altitude and velocity, drogue trigger timer activation, and maximum heat flux.

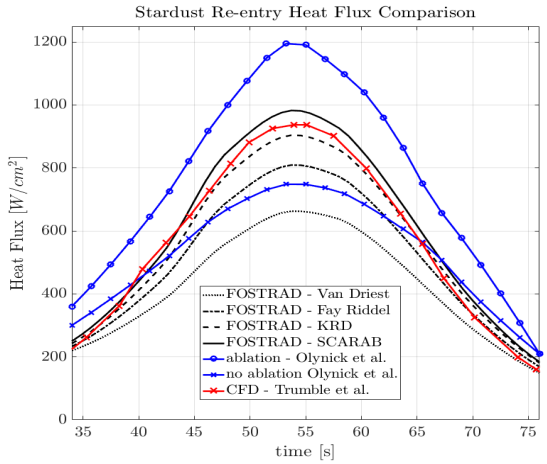

Figure 17: Preliminary validation of FOSTRAD aerothermal models.

of several other possible causes could be the identified in the velocity at the considered altitudes due to different attitudes acquired by the capsule during the re-entry, discrepancies in the atmospheric properties, and errors in the aerodynamic coefficients estimation, or the neglected recession (causing a mass decrement) during the trajectory computation. Neglecting the offset on the altitudes, FOSTRAD and the ablation code underestimate the maximum and average wall temperature of 4.8% and 9.8%, which are deemed to be acceptable under the consideration that the tools are yet low-fidelity and the complete simulation required less than ~ 4 hours.

Another interesting observation can be made on the computed recession distribution, shown in Figure 23. The maximum recession is shown at the stardust nose, and close to the fore-body shoulder. The heat-flux absorbed at close to the shoulder causes an early recession, that progressively increases the exposure of the lee-ward side of the shoulder itself, as it is better shown by the progressive recession in the figures 20 and 21. This particular effect changes also the local surface inclination and radius, increasing and decreasing the local heat-flux. Indeed, the recession on the shoulder causes the angle between the flow and the facets' normals to decrease, inducing an increased heat-flux, in accordance with KRD model[9]. At the same time, the surface geometric variation induces a shoulder-rounding, thus increasing the local radius and decreasing the local heat-flux. The conjunction of these phenomena can only be captured by a constant evolution of the mesh. During the presented study, it has been observed that the accuracy of the geometry evolution changed with the simulation time-step. Indeed, the recession is applied on the mesh "vertexes normals" direction, which are recomputed by FOSTRAD mesh handler at each iteration; thus, highlighting the importance of the real-time coupling between FOSTRAD and the aerothermal ablation code.

6. FOSTRAD USE DISCUSSION

The results obtained for the two test cases have confirmed that, for complex geometries having sharp corners, the local radius formulation provides optimal results if it is initially calibrated on high-fidelity relative heat-flux distributions, as shown in fig. 6-8. Although, in the present study a general rule-of-thumb can be inferred: hemispherical objects (i.e.: Stardust SRC) require a smoothing points density (N_{smooth}) of $\sim$ 3/1000, objects with rounded corners (i.e.: the flat-rounded cylinder) an N_{smooth} of $\sim$ 10/1000, and geometries with sharp-edged corners (i.e.: IXV) an N_{smooth} of $\sim$ 25/1000. In order to prevent discontinuous surface heat-flux distributions, the "flat Edge" parameter, even though it wasn't thoroughly analyzed in the present study, has been observed that it should be set above 0.7.

More in particular, the IXV re-entry study has highlighted the following results: a low-fidelity tool based on the modified Newtonian and adequately integrated with a local nose radius formulation can reliably predict the heat-flux distribution in the continuum regime;

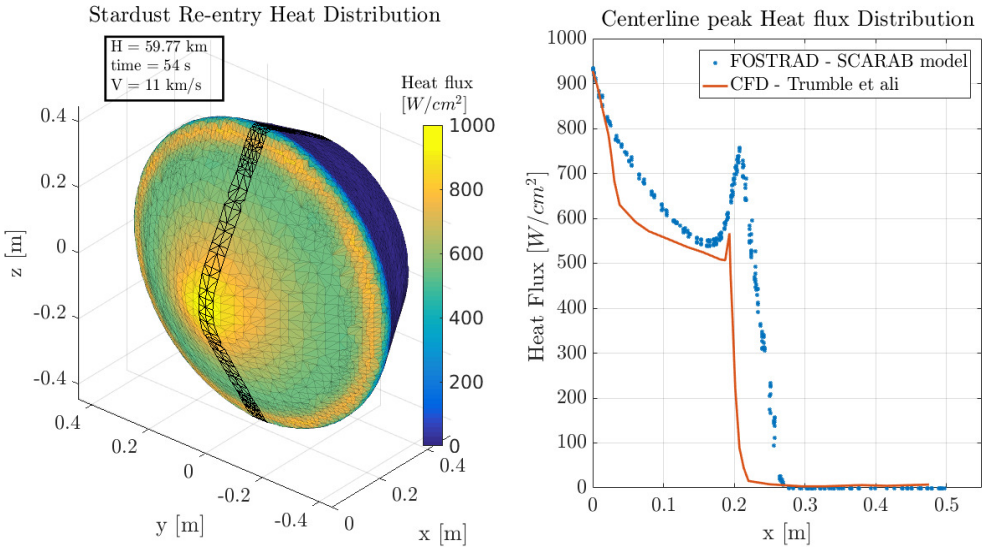

Figure 18: Preliminary validation of FOSTRAD heat-flux surface distribution.

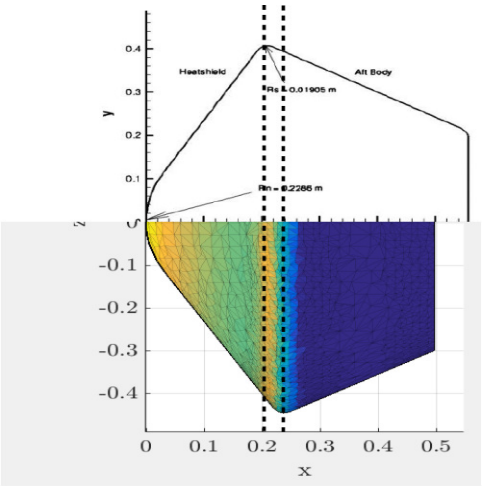

Figure 19: Geometrical differences between the Stardust SRC simulated in the present study(bottom) and the one simulated by Trumble[31](top).

even though significant discrepancies are shown on the surfaces where a shock-impingement or shock-shock interactions take place. Even though, the wall temperature and heat-flux-distribution have shown a qualitatively good agreement with the one preliminary expected by the Catalytic Experiment demonstrator[33]. Indeed, FOSTRAD and the thermal ablation code have shown an underestimation of $\approx 6\%$, and considering the simulation computational time (approximately 1 hour), the results may be considered remarkable.

Moreover, the test on the Stardust SRC has shown that FOSTRAD, employing different aerothermal heating models, can provide reliable heat-flux estimations in the continuum regime. The aerothermal models should be chosen conservatively depending on the field of application, e.g.: design-for-demise or thermal protection system design. The coupling between the thermal ablation code and FOSTRAD has proven to be reliable in terms of recession (fig. 21) estimation, temperature (fig. 22), and geometric evolution. The synchronous coupling between the two codes has proven to be computationally efficient, as the analyses for the entire re-entry of Stardust required a computational time inferior to 4 hours, and granting an underestimation of the predicted maximum wall temperature with respect to experimental data of $\approx 4.8\%$.

7. CONCLUSIONS

The presented work shows the improvements on the Free Open Source Tool for Re-entry of Debris and Asteroids, which has been integrated with a mesh-handler, a local-radius computation algorithm and a trajectory propagator. Additionally, the tool has been coupled with a 1D thermal-ablation code, capable of simulating the structural thermal heat transfer and geometrical recession for ablative materials. The newly implemented local-radius formulation, has been tested on two different problems: the atmospheric re-entry of a lifting body (the intermediate experimental vehicle) and the Stardust Sample Return Capsule.

The study has highlighted that the proposed tool based on low-fidelity models and simplified approaches, can provide reliable and fast results, without having to rely on high performance computer or unaccessible computational power, if all models are adequately integrated.

As near future work, a 6DOF trajectory propagation approach will be evaluated. The tool will be integrated with additional modules such as a multi-bodies handler for satellite and spacecraft nested components, and an altitude break-up estimation model.

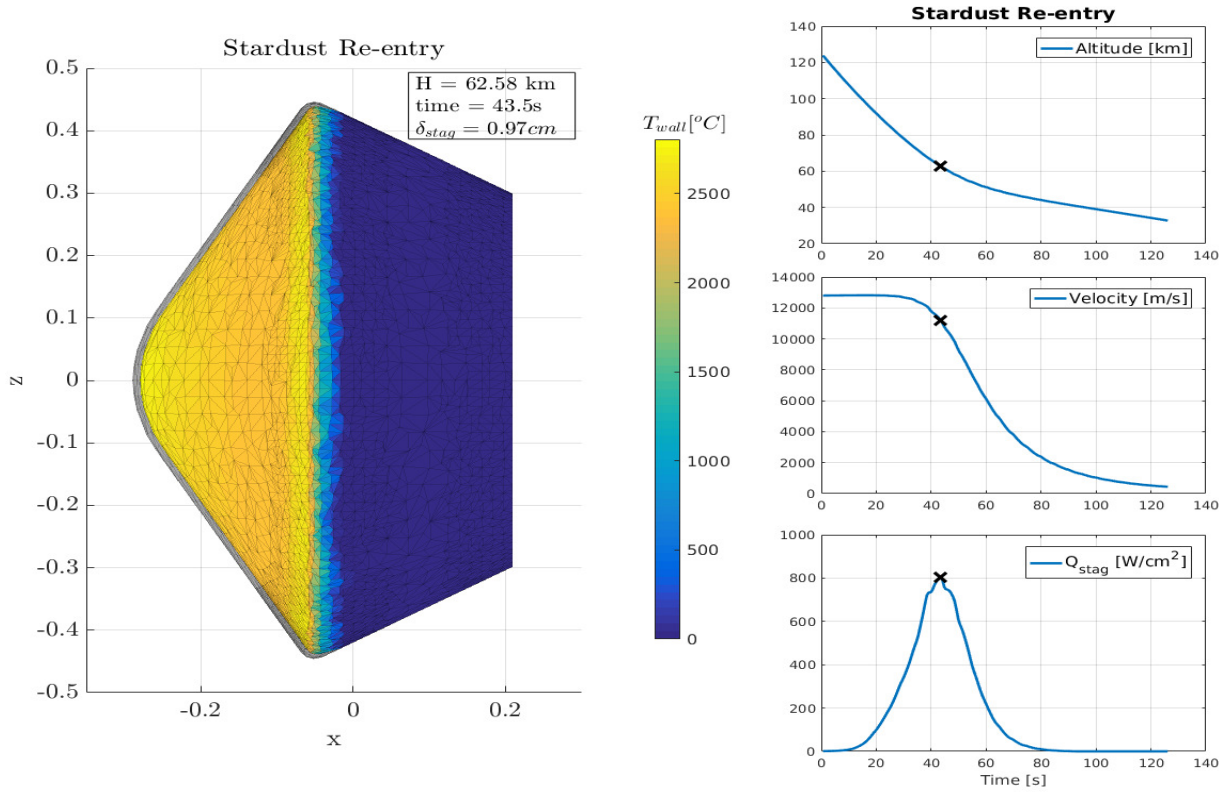

Figure 20: Stardust SRC atmospheric re-entry simulation: recession and temperature distribution at the heat-flux peak. The gray mesh is the initial geometry.

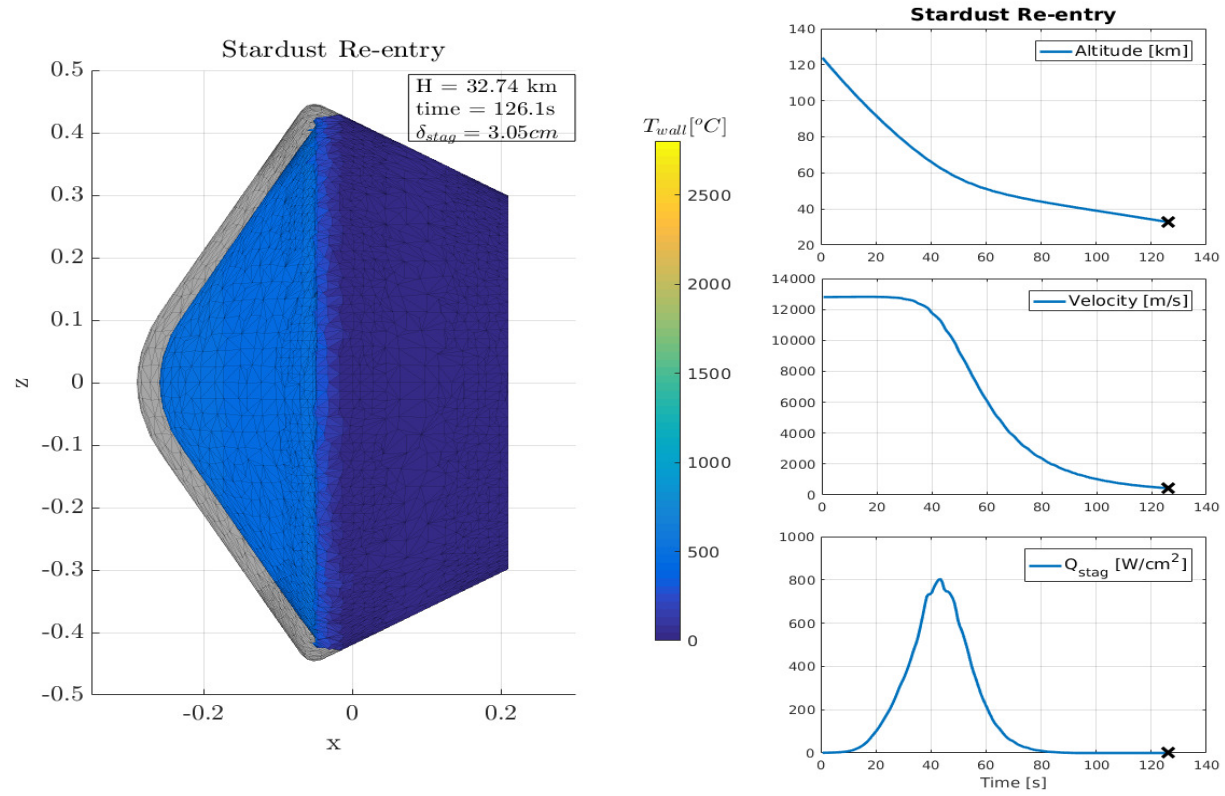

Figure 21: Stardust SRC atmospheric re-entry simulation: final time(before the hypersonic drogue opening triggers).

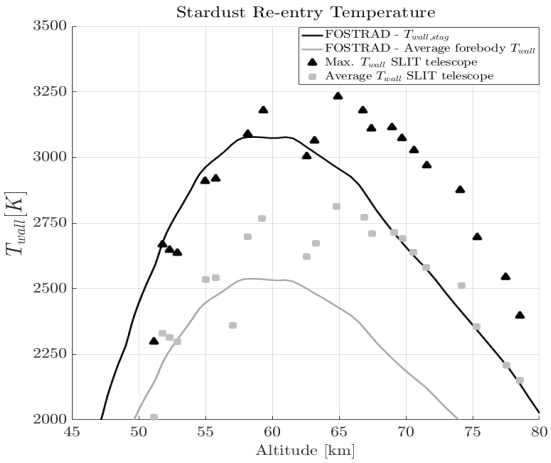

Figure 22: Comparison of Stardust re-entry maximum and averaged wall temperature over altitude, computed with FOSTRAD and observed with the SLIT telescope[35].

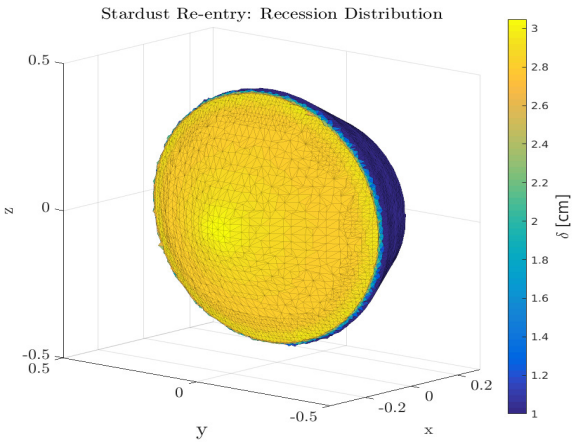

Figure 23: Stardust SRC predicted recession distribution at the hypersonic drogue opening time.

ACKNOWLEDGMENTS

The authors would like to state that the results were obtained using the EPSRC funded ARCHIE-WeSt High Performance Computer (www.archie-west.ac.uk). EPSRC grant no. EP/K000586/1.

REFERENCES

1. Annaloro, J., Omaly, P., Rivola, V., and Spel, M. (2014). Elaboration of a new spacecraft-oriented tool: Pampero. In *Proceedings of the 8th European Symposium on Aerothermodynamics for Space Vehicles*.
2. Couchman, B. and Haynes, M. (2015). Navier-stockes computations for hollow cylinders and cubes relevants for satellite debris. In *Proceedings of the 8th European Symposium on Aerothermodynamics for Space Vehicle*.
3. Desai, P. N. and Qualls, G. D. (2010). Stardust entry reconstruction. *Journal of Spacecraft and Rockets*, 47(5):736.
4. Dogra, V. K., Wilmoth, R. G., and Moss, J. N. (1992). Aerothermodynamics of a 1.6-meter-diameter sphere in hypersonic rarefied flow. *AIAA journal*, 30(7):1789–1794.
5. Donaldson, N., Ireland, P., and Merrifield, J. (2015). Attitude-dependent thermal flux estimation in the slip regime for geometric primitives towards the improvement of destructive re-entry simulations.
6. Falchi, A., Minisci, E., Vasile, M., and Kubicek, M. (2017a). Aero-thermal re-entry sensitivity analysis using dsmc and a high dimensional model representation-based approach. In *7th European Conference on Space Debris*.
7. Falchi, A., Minisci, E., Vasile, M., Rastelli, D., and Bellini, N. (2017b). Dsmc-based correction factor for low-fidelity hypersonic aerodynamics of re-entering objects and space debris. In *7th European Conference for Aeronautics and Space Sciences*, pages 1–15.
8. Kemp, N. H. (1959). Laminar heat transfer around blunt bodies in dissociated air. *Journal of the aerospace sciences*, 26(7):421–430.
9. Kemp, N. H. and Riddel, F. R. (1957). Heat transfer to satellite vehicles re-entering the atmosphere. *Journal of Jet Propulsion*, 27(2):132–137.
10. Klett, R. D. (1964). Drag coefficients and heating ratios for right circular cylinders in free-molecular and continuum flow from mach 10 to 30. Technical report, Sandia Corp., Albuquerque, N. Mex.
11. Koppenwallner, G., Fritsche, B., Lips, T., and Klinkrad, H. (2005). Scarab-a multi-disciplinary code for destruction analysis of space-craft during re-entry. In *Fifth European Symposium on Aerothermodynamics for Space Vehicles*, volume 563, page 281.
12. Lees, L. (1956). Laminar heat transfer over blunt-nosed bodies at hypersonic flight speeds. *Journal of Jet Propulsion*, 26(4):259–269.
13. Lips, T. and Fritsche, B. (2005). A comparison of commonly used re-entry analysis tools. *Acta Astronautica*, 57(2):312–323.

14. Maddock, C. and Minisci, E. (2016). Spaceplane trajectory optimisation with evolutionary-based initialisation.

15. Max, N. (1999). Weights for computing vertex normals from facet normals. *Journal of Graphics Tools*, 4(2):1–6.

16. Mehta, P., Minisci, E., Vasile, M., Walker, A. C., and Brown, M. (2015a). An open source hypersonic aerodynamic and aerothermodynamic modelling tool. In *8th European Symposium on Aerothermodynamics for Space Vehicles*.

17. Mehta, P. M., Kubicek, M., Minisci, E., and Vasile, M. (2016). *Debris re-entry modeling using high dimensional derivative based uncertainty quantification*, volume 156 of *Advances in Astronautical Sciences*, pages 3993–4011. American Astronautical Society.

18. Mehta, P. M., Walker, A., Brown, M., Minisci, E., and Vasile, M. L. (2015b). Sensitivity analysis towards probabilistic re-entry modeling of spacecraft and space debris. In *AIAA Modeling and Simulation Technologies Conference*, page 3098.

19. Merrifield, J., Beck, J., Markelov, G., Leyland, P., and Molina, R. (2015). Aerothermal heating methodology in the spacecraft aerothermal model (sam). In *Space Safety is No Accident*, pages 463–468. Springer.

20. Milos, F. S., Chen, Y.-K., Congdon, W. M., and Thornton, J. M. (1999). Mars pathfinder entry temperature data, aerothermal heating, and heatshield material response. *Journal of Spacecraft and Rockets*, 36(3):380–391.

21. Mitcheltree, R., DiFulvio, M., Horvath, T., and Braun, R. (1999). Aerothermal heating predictions for mars microprobe. *Journal of spacecraft and rockets*, 36(3):405–411.

22. Moyer, C. B. and Wool, M. R. (1970). Aerotherm Charring Material Thermal Response and Ablation Program, Version 3. Volume 1. Program Description and Sample Problems. Technical report, AEROTHERM CORP MOUNTAIN VIEW CA.

23. Olynick, D., Chen, Y.-K., and Tauber, M. E. (1999). Aerothermodynamics of the stardust sample return capsule. *Journal of Spacecraft and Rockets*, 36(3):442–462.

24. Renato, V., Scanlon, T., and Brown, R. (2017a). Multi-dimensional ablation and thermal response program for martian entry analysis. *68th International Astronautical Congress*.

25. Renato, V., Scanlon, T., and Brown, R. (2017b). Multi-dimensional ablation and thermal response program for re-entry analysis. *31st International Symposium on Space Technology and Science*.

26. Rochelle, W. C., Kinsey, R. E., Reid, E. A., Reynolds, R. C., and Johnson, N. L. (1997). Spacecraft orbital debris reentry: Aerothermal analysis.

27. Roncioni, P., Ranuzzi, G., Marini, M., Paris, S., Cosson, E., and Walloschek, T. (2011). Experimental and numerical investigation of aerothermal characteristics of hypersonic intermediate experimental vehicle. *Journal of Spacecraft and Rockets*, 48(2):291.

28. Rusinkiewicz, S. (2004). Estimating curvatures and their derivatives on triangle meshes. In *3D Data Processing, Visualization and Transmission, 2004. 3DPVT 2004. Proceedings. 2nd International Symposium on*, pages 486–493. IEEE.

29. Schaaf, S. and Chambre, P. (1957). Flow of rarefied gases, high speed aerodynamics and jet propulsion, vol. iv, sect. 8.

30. Sun, Z.-X., Tang, Z., He, Y.-L., and Tao, W.-Q. (2011). Proper cell dimension and number of particles per cell for dsmc. *Computers & Fluids*, 50(1):1–9.

31. Trumble, K. A., Cozmuta, I., Sepka, S., Jenniskens, P., and Winter, M. (2010). Postflight aerothermal analysis of stardust sample return capsule. *Journal of Spacecraft and Rockets*, 47(5):765.

32. Van Driest, E. (1956). The problem of aerodynamic heating. *Aeronautical Engineering Review*, pages 26–41.

33. Viladegut, A., Panerai, F., Chazot, O., Pichon, T., Bertrand, P., Verdy, C., and Coddet, C. (2017). Design, integration and preliminary results of the ixv catalysis experiment. *CEAS Space Journal*, 9(2):141–151.

34. Willcockson, W. H. (1999). Stardust sample return capsule design experience. *Journal of Spacecraft and Rockets*, 36(3).

35. Winter, M. W. and Trumble, K. A. (2010). Spectroscopic observation of the stardust re-entry in the near uv with slit: Deduction of surface temperatures and plasma radiation.